Multiple electron transfer in slow Ne^{9+}-Ne collisions

R. Herrmann
Institut für Kernphysik, University of Frankfurt, August Euler Straße 6, 6000 Frankfurt/Main 90, Germany

M. H. Prior
Lawrence Berkeley Laboratory, University of California, Berkeley, 1 Cyclotron Road, Berkeley, California 94720

R. Dörner and H. Schmidt-Böcking
Institut für Kernphysik, University of Frankfurt, August Euler Straße 6, 6000 Frankfurt/Main 90, Germany

C. M. Lyneis
Lawrence Berkeley Laboratory, University of California, Berkeley, 1 Cyclotron Road, Berkeley, California 94720

U. Wille
Hahn-Meitner-Institut Berlin, Glienicker Straße 100, 1000 Berlin 39, Germany
(Received 13 March 1992)

Multielectron transfer probabilities in 90-keV Ne^{9+}-Ne collisions have been measured with respect to the projectile scattering angle θ in a range between $\theta = 12$ and 75 mrad. The projectile final charge state was determined in coincidence with the target-ion final charge state using a time-of-flight technique. For $\theta > 45$ mrad, projectile and target undergo a complete equilibration of their atomic shells (including the K shell) leading to the excitation of both collision partners and the autoionization of three electrons on average. A comparison of the measured final charge-state distributions of projectile and target with those obtained in a former experiment with the system 90-keV Ne^{7+}-Ne [H. Schmidt-Böcking *et al.*, Phys. Rev. A **37**, 4640 (1989)] leads to the conclusion that L- and K-shell charge transfer can be treated as independent processes. Interference structure in the K-K vacancy-transfer probabilities has been observed in the final charge-state probabilities of the "heavy-ion"–atom system.

PACS number(s): 34.70.+e

INTRODUCTION

Electron-transfer reactions are among the most important processes in nature. Almost every chemical reaction is based upon electron and energy transfer between the reaction partners.

Charge-transfer reactions between highly charged ions and atoms are also important processes in many types of plasmas [1]. The composition of hot astrophysical plasmas can be investigated by observation of x-ray emission following electron transfer between the ions in the plasma. A detailed knowledge of the mechanisms and cross sections of those capture reactions would improve the understanding of astrophysical emission spectra.

In confined fusion plasmas, x-ray and electron emission are important cooling processes. In order to control the plasma, a quantitative understanding of reactions leading to x-ray or electron emission—especially of collisions between highly charged impurity ions with light neutrals—is necessary [2]. Furthermore, collisions of highly charged ions with atoms open a large number of reaction channels which can give very detailed information about the collision process itself. Therefore, charge exchange between highly charged ions and atoms has been extensively studied for a wide range of collision systems and collision energies.

Several reviews on the characteristic features of electron capture by multiply charged ions have been given in the past; for example, those by A. Niehaus [3,4], M. Barat *et al.* [5], Janev and Winter [6], Salzborn and Mueller [7], and R. Schuch [8]. Very recently, L. Anderson summarized several publications on studies of slow charge-exchange collisions between multiply charged ions and atoms [2]. Mechanisms for charge transfer at asymptotically high impact velocities were treated in a review article by Shakeshaft and Spruch [9].

An electron-transfer process is, in general, a many-particle Coulomb problem. Since an exact analytical solution for this problem is impossible, several models have been proposed to describe approximately charge transfer between two collision partners. In this context, a distinction between "low" and "high" projectile velocities is required. At "low" projectile velocities the transferred electron can follow the slowly changing two-center potential of projectile and target because the projectile velocity is lower than the mean velocity of the considered electron ($v_P < v_e$). At "high" projectile velocities ($v_P > v_e$) the electron cannot adapt to the rapidly changing projectile-target potential.

For "low" projectile velocities the simplest description for electron transfer is certainly the "classical overbarrier" model [10,4]. According to this model, electron transfer is assumed to take place when the effective Coulomb barrier between the collision partners is de-

creased to a level at which electron transfer classically becomes possible.

A more sophisticated description is given by the "quasimolecular promotion model," introduced by Fano and Lichten [11]. It is based on the assumption that the atomic orbitals of projectile and target form quasimolecular orbitals in the region of small internuclear distances. A theoretical description is obtained within the independent-particle model, taking into account the electron-electron interaction implicitly by calculating an effective one-electron two-center potential. This can be done by applying various methods, such as, for example, the "variable screening" [12] or Hartree-Fock [13] method. The knowledge of the effective one-electron potential allows the determination of energy eigenvalues and wave functions for each electronic single-particle orbital as a function of the internuclear distance; the energies are typically presented in the well-known correlation diagrams. (See, for example, Refs. [12] and [13].) Within this theory, electron excitation and transfer can be described by dynamically induced transition processes between the quasimolecular orbitals. The amplitudes for such quasimolecular electronic transitions depend strongly on the spatial overlap and the energy spacing of the two involved orbitals. In a collision these parameters are determined by the projectile's trajectory relative to the target. Thus the electron-transfer probabilities show a strong dependence on the minimum internuclear distance. An experimental access to this characteristic parameter in a collision event can be obtained by a measurement of the projectile scattering angle θ.

Even though experimental data for θ differential electron transfer probabilities can yield very sensitive tests of the molecular-orbital (MO) promotion models, very few θ differential multiple electron-transfer measurements have been done in the low-velocity regime. The first coincidence scattering experiment, studying Ar^+-Ar collisions in an energy range between 12 and 50 keV, was reported by Afrosimov *et al.* [14]. Very similar measurements at the same collision system at incident energies between 3 and 400 keV have been performed by Kessel and Everhardt [15]. They studied the outgoing charge states of projectile and target as a function of the inelasticity f, the scattering process (Q value), and the projectile (θ) and target (Φ) scattering angles in a θ range between 8° and 40°. There it was found that the outgoing projectile and target charge states are independent and uncorrelated except in a region where the inelastic energy (Q) shows a double-peak structure. Fano and Lichten [11] explained the observed structure as resulting from an L-shell vacancy that was produced by a quasimolecular promotion mechanism. Consequently, Kessel, McCaughey, and Everhardt [16] interpreted a very similar double-peak structure of the Q value in the Ne^+-Ne system as resulting from a K vacancy arising also from a quasimolecular promotion.

Applying a very similar technique, Fastrup, Hermann, and Kessel [17] studied the quasimolecular K- and L-vacancy production of several collision systems with respect to the impact parameter and the collision velocity. The impact-velocity dependence of K- and L-shell vacancy production allowed one to identify different quasimolecular promotion mechanisms for both processes.

Based on the assumption that the K-shell vacancy is produced via a rotational-coupling mechanism between the $2p\sigma$ and $2p\pi$ molecular orbitals, Briggs and Macek [18] applied the electron-promotion model of Fano and Lichten [11] to the calculation of the impact-parameter-dependent probability and total cross section of the K-shell-vacancy production in ion-atom collisions. The results of this method showed good agreement with experimental data of Cacak, Kessel, and Rudd [19] for the total cross section of K-vacancy production in the Ne^+-Ne system for impact energies between 50 and 350 keV.

According to Meyerhof [20], the K-vacancy transfer into the higher-Z partner of a near-symmetric ion-atom collision can be explained by the $1s\sigma$-$2p\sigma$ radial-coupling mechanism. Meyerhof derived a universal form for the probability of this transfer process by applying the charge-transfer theory of Demkov.

Some experiments have been performed with He targets investigating single and double electron transfer at very low velocities. In a three-electron system (He^+-He), Aberth *et al.* [21], for example, have measured differential cross sections for charge exchange at a collision energy of 300 eV.

Based on the single-electron-transfer data, multielectron-transfer investigations can help to determine whether the transfer of electrons can be described in an independent-electron model using binomial statistics. Multielectron-transfer cross sections have been measured for high (non-MO) energies by Kraessig *et al.* [22] for the system $F^{9+}+Ne$ at a collision energy of 0.53 MeV/u. Particularly in the energy regime of a few keV/u, the only investigation of differential cross sections of multielectron transfer between highly charged projectile ions and target atoms, resolving the final charge states of the collision partners and the projectile scattering angle, has been performed by Schmidt-Böcking *et al.* for the system 90-keV Ne^{7+} on Ne [23]. That experiment showed that, in collisions where the projectile scattering angle is larger than about 12 mrad, the Ne L shells form a complete quasimolecule, and outgoing collision partners end up with the same mean charge states. It furthermore was observed that in this "low" impact-velocity regime ($v_P/v_e \leq 0.03$), direct ionization of target and projectile is negligible. It was concluded that all electrons lost to the continuum in a scattering process originate from autoionizing processes during or after the collision. Since only final charge states were measured, the Ne^{7+}-Ne experiment did not determine the final orbitals into which the electrons were transferred.

If a $1s$ vacancy is carried into the system, a much more detailed statement is possible for charge transfer between the inner quasimolecular orbitals. In the case of an incoming Ne^{9+} ion, a characteristic oscillating structure in the scattering-angle dependence of the charge-transfer probability is expected when the projectile $1s$ vacancy is transferred to the $1s$ orbital of the target. This well-known [21,24,25] oscillation structure in the K- to K-shell charge-transfer probability can be understood as follows.

A vacancy in the $1s\sigma$ orbital originating from the pro-

jectile K shell can be transferred via radial coupling to the $2p\sigma$ orbital, where the transition amplitude peaks at an internuclear distance of about two times the atomic K-shell radius [26]. As can be seen in Fig. 1, during the collision the radial coupling region is passed on the incoming and on the outgoing part of the trajectory. Since these two transition amplitudes cannot be distinguished experimentally by measuring the total K-vacancy transfer probability, this probability is obtained by a coherent addition of the incoming and outgoing amplitudes. Depending upon the phase difference of the two transition amplitudes, interference will be constructive or destructive. The phase difference depends upon the minimum internuclear distance, which is determined by the impact parameter and collision energy. This means that for fixed energy, at some impact parameters the K vacancy is very likely transferred, while at others the two transition amplitudes interfere destructively, yielding a minimum total transfer probability. Since for fixed projectile energy the projectile scattering angle is a function of the impact parameter, the K-vacancy transfer probability should show an oscillating structure with respect to the projectile scattering angle. Alternatively, an oscillation structure can be expected for a fixed impact parameter as function of the projectile velocity. This interference effect is well established and has first been observed in the K-vacancy transfer probability as a function of the impact velocity in very light collision systems (Ziemba *et al.* [26], Lockwood, Helbig, and Everhardt [27], and Everhardt [28]). An interference structure in the impact-parameter-dependent K-vacancy transfer probability at fixed projectile energies was found with projectiles that carry a K vacancy in the collision (for example, at He^+ on He [21]). The first experiments using heavy ions were performed with S^{15+} [24] and S^{16+} [25,29] colliding with Ar. Later other systems like F^{8+} on Ne [30] were investigated. Single and double K-vacancy transfer as function of the impact parameter was again studied at the system $S^{16+}+Ar$ by Schulz [31].

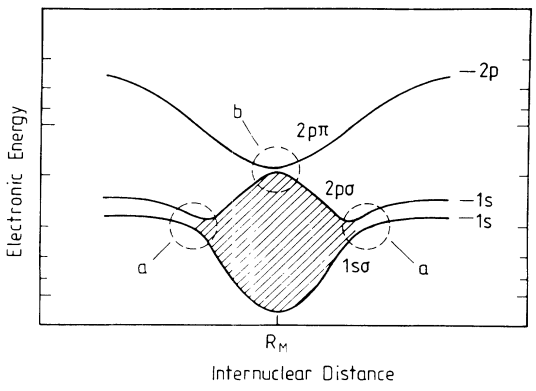

FIG. 1. Schematic correlation diagram of the three innermost quasimolecular orbitals. Electronic energy is plotted vs internuclear distance between projectile and target. R_M indicates the distance of closest approach. The dashed circles labeled *a* show the regions of maximum radial coupling amplitudes between the $1s\sigma$ and $2p\sigma$ quasimolecular orbitals. The region *b* indicates the maximum of the rotational coupling amplitude between the $2p\sigma$ and $2p\pi$ orbitals. The shaded area symbolizes the phase difference between incoming and outgoing amplitude for K-K vacancy transfer.

It is not *a priori* obvious that the described interference effect can also be observed in the present system of 90-keV $Ne^{9+}+Ne$ because the K-vacancy transition amplitude on the incoming part of the trajectory could be very different from that on the outgoing part because of the different K-shell screening due to the transferred L-shell electrons. Furthermore, a vacancy in the projectile L shell can also be transferred via rotational coupling into the target K shell [25] (see Fig. 1). This transition, which couples the $2p\sigma$ and $2p\pi$ quasimolecular orbitals, is due to a transfer of angular momentum from the nuclear motion to the active electron. Kambara *et al.* [32] could show at the $Ne^{7+}+Ne$ system that the rotational coupling between $2p\sigma$ and $2p\pi$ can only populate the $2p\pi_x$ suborbital (its angular momentum vector is perpendicular to the scattering plane). At asymptotically large internuclear distances, the vacancy in the $2p\sigma$ orbital leads to a K-shell vacancy in the target atom. If the strength of this coupling mechanism is comparable to the radial coupling between the two K shells, the K-K interference structure could be smeared out.

Based on the data of the 90-keV $Ne^{7+}+Ne$ experiment [23], the intention of the present investigation was to study the K-vacancy transfer and its possible interferences with the L-shell charge transfer in the Ne-Ne system. This was done by measuring the final charge-state distribution of projectile and target ions with respect to the projectile scattering angle in a range between $\theta=12$ and 75 mrad for incoming Ne^{9+} projectiles colliding with Ne atoms at a collision energy of 90 keV ($v_P/(v_e)_{K\text{ shell}}\approx 0.03$). According to an estimation by using a screened Moliere-type potential [33] for the collision partners, the investigated range of projectile scattering angles corresponds roughly to an impact parameter range between 0.9 and 0.25 a.u.

EXPERIMENTAL ARRANGEMENT AND DATA REDUCTION

The apparatus used in the experiment provided the coincident, charge-sensitive detection of the outgoing projectile and target as well as the projectile scattering angle θ. Figure 2 shows the experimental setup. With three collimators in the beam line in front of the apparatus it was possible to form a beam spot of about 0.02 mm^2. The ion beam collided with the Ne atoms at about 1 mm below the nozzle from which the gas effused. The target area was differentially pumped, keeping the region outside below 2×10^{-6} mbar, while the target pressure could be varied between 1×10^{-5} and 5×10^{-5} mbar. Single-collision conditions were ensured by performing several short test measurements at different target pressures.

A parallel-plate electrode structure, located in the target area, produced a weak horizontal electrostatic field of about 150–200 V/cm perpendicular to the beam axis in order to extract target ions. After passing a grid and a drift tube, these target-recoil ions were detected by a

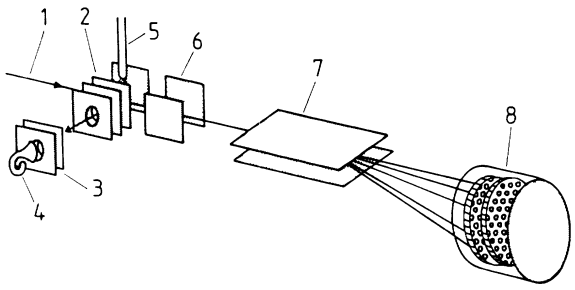

FIG. 2. Sketch of the experimental setup. 1, incoming ion beam; 2, recoil-ion extraction plates; 3, recoil-ion acceleration plates; 4, channeltron for recoil-ion detection; 5, nozzle for target-gas jet; 6, compensating electrostatic deflector; 7, electrostatic deflector for projectile-charge-state separation; 8, position-sensitive channel-plate detector for projectile detection.

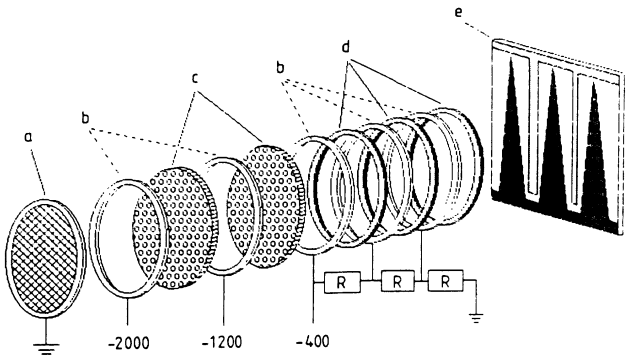

FIG. 3. Sketch of the projectile detector. *a*, grid; *b*, potential rings; *c*, microchannel plates; *d* insulating rings; *e*, wedge and strip anode.

channeltron detector. The charge-state analysis of the recoil ions was obtained by measuring their flight times in the extraction and drift region. The ratio (1:2) between lengths of extraction field and drift region ensured that different starting points of the target ions had a minimum influence on their flight time. The start signal for this time-of-flight (TOF) measurement was obtained from the detector for the scattered projectile ion.

After colliding with the target atoms in the extraction field, the projectile ions traversed a second horizontal electrostatic field of the same strength in the reverse direction compared to the extraction field. This corrected the influence of the extraction field on the charge-exchanged scattered projectiles.

The scattered projectile ions were charge analyzed by separation in a third electrostatic field produced by two horizontal parallel plates, which dispersed the different charge states in the vertical direction. At a distance of about 30 cm from the analyzer plates the charge state separated, and scattered projectiles were detected by a two-dimensional position-sensitive channel plate detector. The projectile position was determined by using a "wedge and strip anode" (Ref. [23]). In order to obtain a high ratio between signal and noise, which improves the position resolution, the detector operated with two channel plates in series. Figure 3 shows schematically the design of the particle detector.

A vertical strip mask in front of the detector limited the smallest measurable projectile scattering angle to $\theta \approx 12$ mrad; this allowed counting higher particle rates in the interesting scattering angle range between 12 and 75 mrad. This mask could be moved away in order to find the position of $\theta = 0$ for each final projectile charge state using attenuated beam intensity.

The electronic setup used in the experiment is equivalent to that described in Ref. [23]. For each data event four parameters (one TOF coordinate, three projectile position coordinates) were collected by a multiparameter computer system and written as list-mode data on magnetic tape for off-line analysis.

The position information from the projectile detector recorded as x-y coordinates was transformed to R-φ_p coordinates for every final projectile charge state. R describes the distance from the position where $\theta = 0$, and φ_p is the azimuthal projectile scattering angle. The scattering angle was obtained from the R coordinate and the distance between the collision region and the particle detector. Figure 4 shows the two-dimensional projection of a time-of-flight spectrum versus the projectile scattering angle (arbitrary units) for the projectile charge state $Q = 7+$. The true-coincidence events for the different recoil-ion charge states q can clearly be separated as different "bands" in this plot. It can be seen that the flight time of the recoil ions decreases with increasing θ. This is due to the increasing momentum transfer from the projectile to the recoil ion with rising θ, yielding a higher initial velocity of the recoil ions in the extraction field. This effect was compensated for in the data reduction by shifting the TOF coordinate with respect to the θ coordinate so that the true coincidence events form "bands" parallel to the θ axis. Figure 5 shows a two-

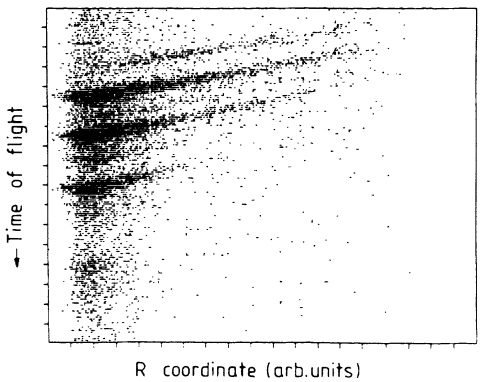

FIG. 4. Two-dimensional projection spectrum of target-recoil-ion time of flight vs projectile R coordinate on the microchannel plate detector for the final projectile charge state $Q = 7+$. ($R = L \tan\Theta$, where L describes the distance between gas target and projectile detector.)

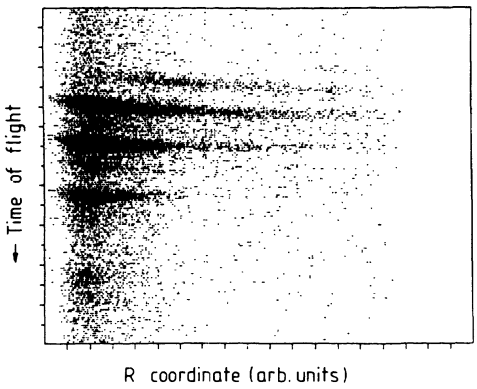

FIG. 5. Same as Fig. 4, except the TOF coordinate is shifted to smaller values of the R coordinate to correct for the R-dependent momentum transfer from the projectiles to the target ions (see text).

dimensional (2D) θ-TOF spectrum which is modified in the described way. After this modification it was possible to perform projections out of the 2D spectrum onto the θ axis for each recoil-ion charge state. The time-of-flight spectrum in Fig. 6 (integrated over all θ and projectile charge states) shows the true coincidences sitting on a random background. Thus the background correction for a 2D θ-TOF spectrum was done by determining the random coincidences within a window outside the peak region, and subtracting these proportionally from the entire θ-TOF spectrum. The identification of the different TOF peaks (the assignment of each TOF peak with a recoil-ion charge state) was done by using the relation

$$t_R = D\frac{1}{\sqrt{q}} , \tag{1}$$

where t_R is the recoil-ion flight time, q its charge state, and D a constant (see Ref. [23]).

The number of true coincidences $N_{\text{true}}(q,Q,\theta)$ for each final target charge state q, projectile charge state Q, and projectile scattering angle θ is given by

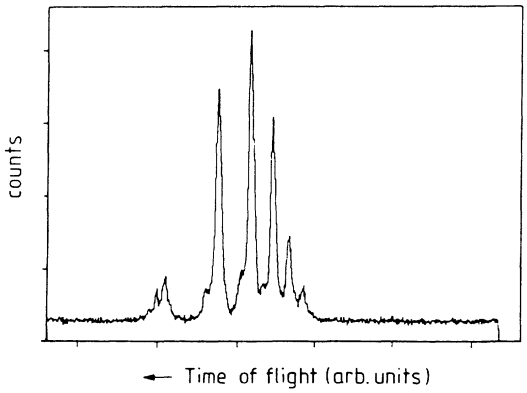

FIG. 6. Typical time-of-flight spectrum integrated over all projectile scattering angles θ and projectile final charge states Q.

$$N_{\text{true}}(q,Q,\theta) = N_p\rho\frac{d\sigma}{d\theta}P(q,Q,\theta)\frac{\Delta\Omega_{\text{eff}}}{\sin\theta\Delta\Phi} . \tag{2a}$$

$P(q,Q,\theta)$ describes the probability that in a collision event a projectile ion with charge state Q is scattered in the angle θ, while a target ion with charge state q is produced. N_p describes the number of incoming ions, ρ is the target density (in atoms per cm^2), $d\sigma/d\theta$ is the singly differential scattering cross section, $\Delta\Phi$ and $\Delta\theta$ are the geometric azimuthal and polar angles, and $\Delta\Omega_{\text{eff}}$ is the effective solid angle of the projectile detector. $\Delta\Omega_{\text{eff}}$ is given by $\Delta\Omega_{\text{eff}} = \sin\theta\Delta\theta\Delta\Phi_{\text{eff}}$, so that Eq. (2a) can be written as

$$N_{\text{true}}(q,Q,\theta) = N_p\rho\frac{d\sigma}{d\theta}P(q,Q,\theta)\Delta\theta\frac{\Delta\Phi_{\text{eff}}}{\Delta\Phi} . \tag{2b}$$

As will be shown below, $\Delta\Phi_{\text{eff}}$ is not equivalent with $\Delta\Phi$ but is a function of q and θ.

The quantities N_p, ρ, $\Delta\theta$, and $d\sigma/d\theta$ can be combined to $C(\theta)$:

$$N_p\rho\frac{d\sigma}{d\theta}\Delta\theta = C(\theta) . \tag{3}$$

Differential capture probabilities could be measured for projectile charge states between $Q=5+$ and $Q=8+$, while the final target ions had charge states between $q=3+$ and $q=8+$. There were also an extremely small number of projectiles with charge states $Q=9+$ and $Q\leq 4+$ observed; these were neglected in the data analysis. Thus to a very good approximation

$$\sum_{q,Q} P(q,Q,\theta) = 1 , \tag{4}$$

where q includes values between $3+$ and $8+$ and Q between $5+$ and $8+$. Thus, from Eqs. (2b), (3), and (4) one has

$$P(q,Q,\theta) = \frac{N_{\text{true}}(q,Q,\theta)\Delta\Phi}{\Delta\Phi_{\text{eff}}C(\theta)} , \tag{5}$$

$$\sum_{q,Q} N_{\text{true}}(q,Q,\theta) = \frac{\Delta\Phi_{\text{eff}}C(\theta)}{\Delta\Phi} . \tag{6}$$

The geometrical solid angle $\Delta\Omega_{\text{geo}}$ in which a recoil ion can be detected in coincidence with a scattered projectile ion is given by $\Delta\Omega_{\text{geo}} = \Delta\vartheta\sin\vartheta\Delta\varphi$. Here ϑ and φ describe the polar and azimuthal recoil-ion scattering angles, where $\vartheta=\pi/2$, $\varphi=0$ defines the direction into the channeltron (see Fig. 2).

For the investigated range of projectile scattering angles, the transverse momenta of the autoionized electrons are negligible relative to the transverse recoil ion and projectile momenta. Thus the collision is perfectly described by two-body kinematics, so that the relative polar and azimuthal angles between a scattered projectile ion and a recoil ion is always given by $\vartheta-\theta=\pi/2$ and $\Phi-\varphi=\pi$. So the recoil-ion scattering angle ϑ and azimuthal angle φ are given by $\vartheta=\pi/2-\theta$ and $\varphi=\Phi-\pi$.

The ϑ range for the detection of recoil ions was limited by the geometry of the projectile detector yielding $\vartheta_{\min}=\pi/2-12$ mrad to $\vartheta_{\max}=\pi/2-80$ mrad. Within

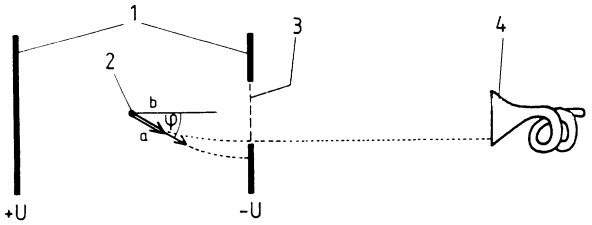

FIG. 7. Illustration of the dependence of the maximum azimuthal angle φ_{max} on the initial velocity of the recoil ion. The recoil ions *a* and *b* are produced within the extraction plates (1) at the position of the ion beam (2). Both are scattered in the same azimuthal angle φ and have the same charge state q. Ion *a* has an initial velocity too high in order to be deflected through the grid (3). The velocity of recoil ion *b* is small enough so that the excitation field can deflect it into the channeltron electron multiplier (4).

this range of scattering angles, the range of azimuthal angles $\Delta\varphi=\Delta\Phi$ for which a recoil ion could be detected coincidently with a scattered projectile ion is exclusively determined by the recoil-ion spectrometer. This can be understood by the following analysis: Because of the extraction field E_R in the recoil spectrometer, the maximum azimuthal angle φ_{max} depends on the initial velocity of the recoil ion. This is illustrated in Fig. 7. (In the case of $E_R=0$, φ_{max} would be identical with the geometric maximum azimuthal angle φ_{geo}.)

In collision processes with large projectile scattering angles a relatively large amount of transverse momentum is transferred from the projectile to the recoil ion. For these recoil ions the velocity gain in the extraction field can be neglected relative to their initial velocity. Their path in the spectrometer is described to a very good approximation by a straight line in the direction of their initial velocity. Thus for these fast ions φ_{max} is almost equivalent to φ_{geo}. Fast recoil ions can only pass the spectrometer exit and be detected in the channeltron when they are scattered in azimuthal angles φ which are smaller than φ_{geo}. Recoil ions to which the projectile transferred only a small amount of transverse momentum start with relatively small velocities. Their motion in the spectrometer is strongly influenced by the extraction field so that even ions that are scattered in azimuthal angles larger than φ_{geo} can be deflected through the spectrometer exit.

The initial recoil-ion velocity depends only on the projectile scattering angle θ. The velocity gain in the extraction field is a function of the recoil-ion charge state q. Thus the maximum azimuthal angle for which a recoil ion can be detected depends on the recoil-ion charge state q and the scattering angle of the coincidently measured projectile ion θ. The correct mathematical relation for φ_{max} is given implicitly by the following formula:

$$\frac{[r_{ch}^2-(S_1+S_2)^2\tan^2\theta]^{1/2}}{v_p\tan\theta\sin(\varphi_{max})} = \left[[K\tan\theta\cos(\varphi_{max})]^2+\frac{2KS_1}{v_p}\right]^{1/2}-K\tan\theta\cos(\varphi_{max}) +S_2\left[[v_p\tan\theta\cos(\varphi_{max})]^2+\frac{2qeE_{ex}S_1}{m}\right]^{-1/2}, \quad (7)$$

where $K=v_p m/E_{ex}qe$, r_{ch} is the radius of the channeltron cone, v_p is the initial projectile velocity, S_1 is the length of the recoil-ion acceleration path, S_2 is the length of the recoil-ion drift path, E_{ex} is the recoil-ion extraction field, m is the recoil-ion mass, q is the recoil-ion charge state, and e is the unit charge. From this relation φ_{max} was calculated numerically as a function of the recoil-ion charge state q and the projectile scattering angle θ. Figure 8 shows φ_{geo} and calculated values of $\varphi_{max}(q,\theta)$ as a function of θ for the recoil-ion charge states between $q=3+$ and $7+$.

Taking into account that $\Delta\Phi=\Delta\varphi=2\varphi_{max}$, the following expression for $P(q,Q,\theta)$ can be derived from Eqs. (5) and (6):

$$P(q,Q,\theta)=\frac{N_t(q,Q,\theta)/\varphi_{max}(q,\theta)}{\sum_{q,Q}[N_t(q,Q,\theta)/\varphi_{max}(q,\theta)]}. \quad (8)$$

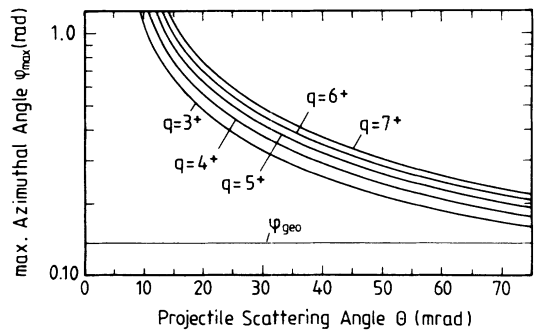

FIG. 8. φ_{max} as function of the projectile scattering angle θ for the recoil-ion charge states between $q=3+$ and $7+$. The line parallel to the abscissa indicates the maximum geometric azimuthal angle $\varphi_{geo}=0.13$ rad.

RESULTS AND DISCUSSION

Figures 9(a)–9(e) show the final charge-state distributions of projectile and target ions at the projectile scattering angles $\theta=16$, 30, 46, 60, and 75 mrad. The squares represent the target ions, while the triangles describe the final projectile ions. As Fig. 9(a) shows, for $\theta=16$ mrad, the maxima of the projectile- and recoil-ion distributions differ by three charge units. The mean final projectile charge state at that angle is $Q=7+$ while the recoil ions have on average the charge state $q=4+$. With increasing scattering angle, the distributions become more and more similar. It can be seen that for $\theta=46$, 60, and 75 mrad, the recoil and projectile ions leave the collision on the average with the same charge of about $5+$ and $6+$, respectively. This is a strong indication that for scattering angles larger than $\theta=46$ mrad a complete quasi-

molecular system including the two K shells is formed during the collision. On the average, three–four autoionization electrons are lost after each collision, indicating that the partners leave the collision in highly excited states.

Figure 10(a) shows again the charge-state distributions for outgoing projectile and recoil ions at $\theta=16$ mrad for the system measured here and additionally those measured in the Ne^{7+}-Ne experiment [23]. The two recoil-ion distributions are almost identical, while the shapes of the outgoing projectile-ion distributions look very similar but are shifted by about $2\frac{1}{2}$ charge states relative to each other. This can be explained as follows: As a result of the Ne^{7+}-Ne measurements, it is known that, due to the relatively small total collision energy of 90 keV, direct ionization does not contribute to the charge exchange of the collision partners. Furthermore, at $\theta=16$ mrad the two K shells do not form quasimolecular states. Thus the K vacancy is expected to remain with the projectile during the collision.

The K vacancy counts for one additional initial projectile charge unit in the present measurement compared to the Ne^{7+}-Ne experiment. Taking into account that the K-shell vacancy has a probability of nearly one for decay by autoionization after the collision, one can state that in the $Ne^{9+}+Ne$ collision system the projectile loses on average one more electron after the collision by decay of the K vacancy than in the $Ne^{7+}+Ne$ system. Assuming that the L-shell charge transfer does not depend on the initial occupation of the two K shells, one could expect that the L-shell electrons are shared between projectile and target during the collision as it was observed in the Ne^{7+} measurement. Since the Ne^{9+} projectile enters the collision with one more L vacancy than the Ne^{7+} projectile, one should expect that on average half of the L vacancy should remain with the final projectile. Thus one could conclude that the final charge-state distribution of the projectiles in the Ne^{9+} experiment should be on average $2\frac{1}{2}$ units higher than in the Ne^{7+} experiment. Figure 10(b) confirms this conclusion. Here the projectile final charge-state distribution from the Ne^{7+} experiment is shifted to higher charge states by three units. One sees that the final projectile charge distribution of the Ne^{9+}-Ne experiment is in very good agreement with the shifted distribution from the Ne^{7+}-Ne experiment. Based on this comparison, one can state that in distant collisions, where no K-K transfer can occur, the projectiles $1s$ vacancy is acting as a spectator without affecting the outer-shell charge exchange. This result supports the assumption that in collision systems similar to the one investigat-

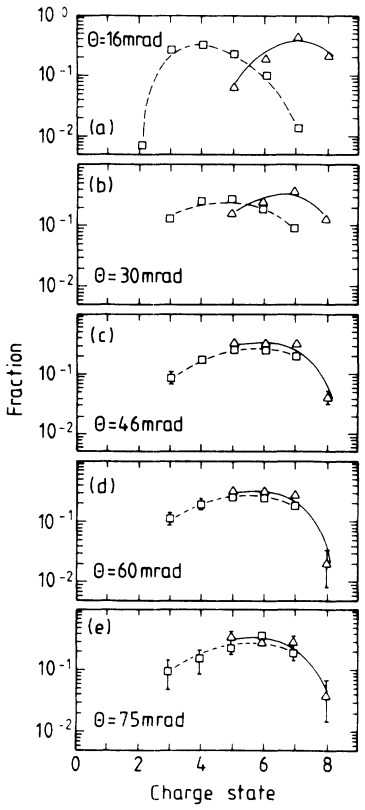

FIG. 9. Final charge-state distributions of projectile and target ions at five different projectile scattering angles θ. The squares represent the target ions, while the triangles describe the final projectile ions. The solid and dashed lines in the spectra are drawn to guide the eye.

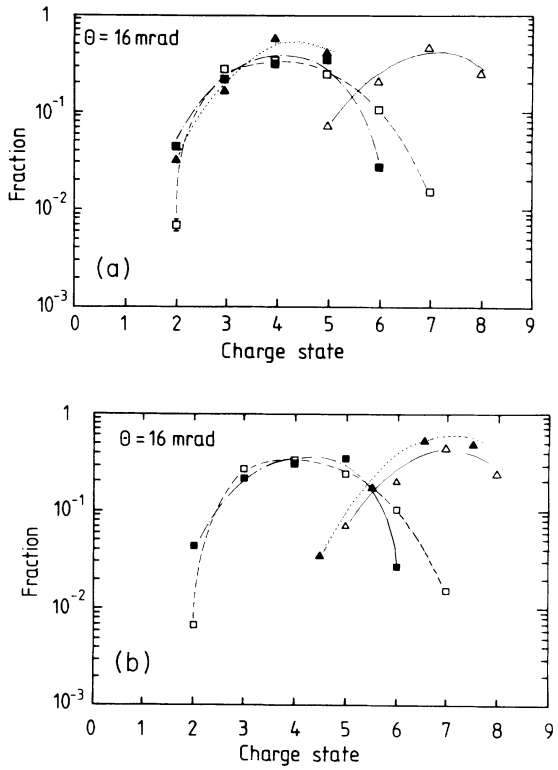

FIG. 10. (a) Final charge-state distributions of projectile and recoil ions at the projectile scattering angle $\theta=16$ mrad. Squares represent the target ions and triangles the projectile ions. The open symbols are results from this experiment, the solid symbols show the results from the Ne^{7+}-Ne experiment (see Ref. [14]). (b) Same as (a) except the final projectile distribution of the Ne^{7+}-Ne experiment [23] is shifted $2\frac{1}{2}$ units higher in charge.

TABLE I. List of intermediate channels that lead to the measured charge-state combination $(q,Q)=(5+,7+)$. The collision partner that carries the K vacancy after the collision is marked with a (K), while an asterisk indicates an excited outer-shell state that is supposed to decay via autoionization. The subscripts at the symbols for the autoionized electrons indicate from which collision partner (P or T) and out of which shell (K or outer) they are emitted.

Process
$Ne_P^{9+}+Ne_T \rightarrow Ne_P^{6+}(K)+Ne_T^{**3+} \rightarrow Ne_P^{7+}+Ne_T^{5+}+2e_{ou,T}+e_{KP}$
$Ne_P^{9+}+Ne_T \rightarrow Ne_P^{*5+}(K)+Ne_T^{*4+} \rightarrow Ne_P^{7+}+Ne_T^{5+}+e_{ou,T}+e_{ou,P}+e_{KP}$
$Ne_P^{9+}+Ne_T \rightarrow Ne_P^{**4+}(K)+Ne_T^{5+} \rightarrow Ne_P^{7+}+Ne_T^{5+}+2e_{ou,P}+e_{KP}$
$Ne_P^{9+}+Ne_T \rightarrow Ne_P^{7+}+Ne_T^{**2+}(K) \rightarrow Ne_P^{7+}+Ne_T^{5+}+2e_{ou,T}+e_{KT}$
$Ne_P^{9+}+Ne_T \rightarrow Ne_P^{*6+}+Ne_T^{+3+}(K) \rightarrow Ne_P^{7+}+Ne_T^{5+}+e_{ou,T}+e_{ou,P}+e_{KT}$
$Ne_P^{9+}+Ne_T \rightarrow Ne_P^{**5+}+Ne_T^{4+}(K) \rightarrow Ne_P^{7+}+Ne_T^{5+}+2e_{ou,T}+e_{KT}$

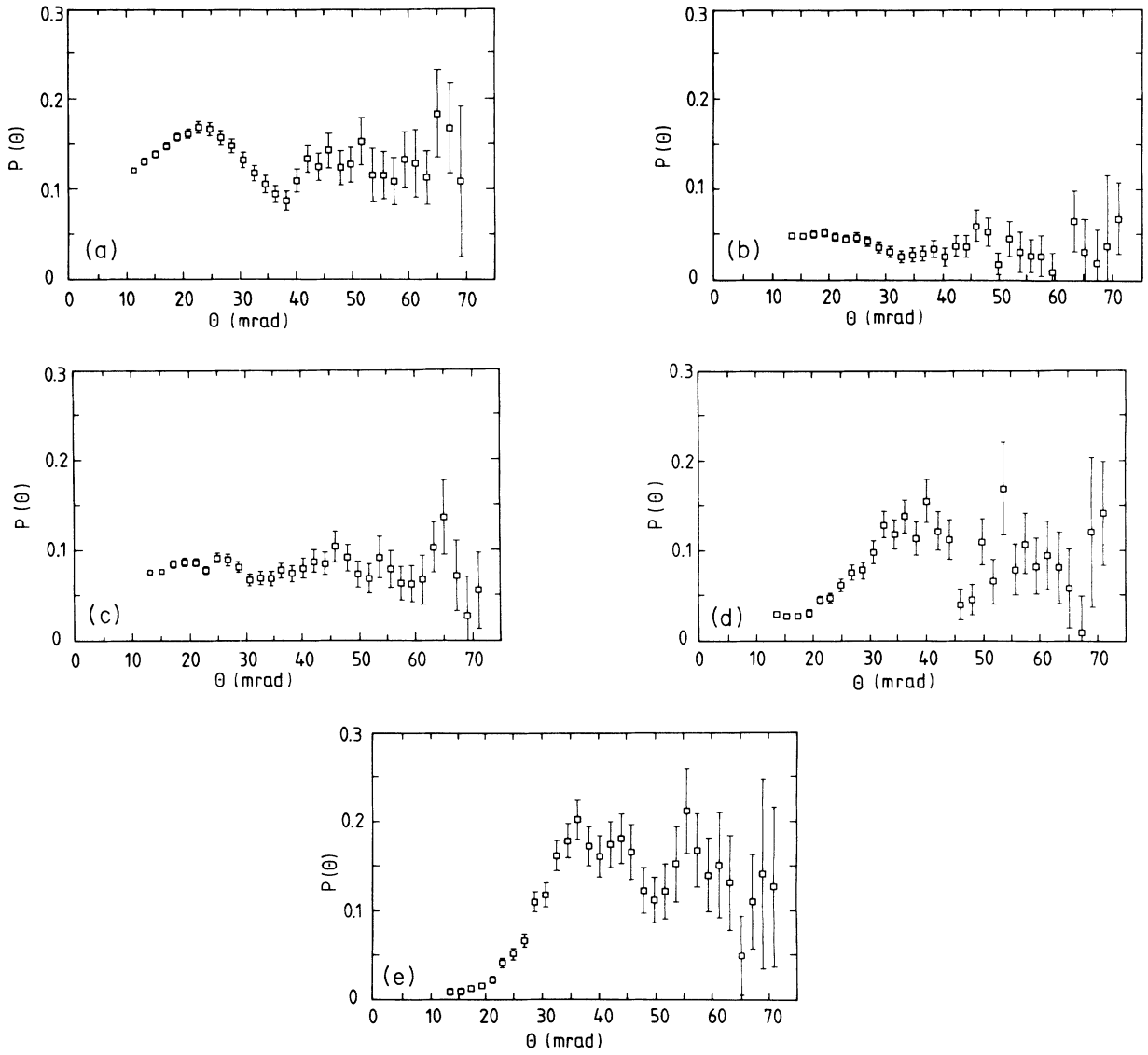

FIG. 11. $P(q,Q,\theta)$ vs the projectile scattering angle θ for those final charge-state combinations (q,Q) where oscillation structures can be observed. (a) (5+,7+), (b) (4+,6+), (c) (5+,6+), (d) (6+,5+), (e) (7+,5+).

ed here L- and K-shell charge transfer may occur independently. Further analysis below yields more evidence for this statement.

Figures 11(a)–11(e) show the scattering-angle-dependent probabilities $P(q,Q,\theta)$ of those final projectile- and target-ion charge-state combinations where oscillation structures were observed. The $P(q,Q,\theta)$ of all other measured charge-state combinations are shown in the Appendix. They show, within the experimental uncertainty, no oscillations.

The following qualitative analysis argues that the observed oscillations in the spectra of Figs. 11(a)–11(e) can be explained well by the expected KK interference effect. Furthermore, it will become clear why the oscillation structures appear selectively only in the spectra of some final charge-state combinations of projectile and target.

First, one has to consider autoionization processes occurring in target and projectile just after the collision but before their detection in the channeltron and channelplate detector. To every measured set (q,Q) one can attach all possible "intermediate states" which are defined as the charge-state combinations of projectile and recoil ion just after the collision before autoionization occurs. An analysis of all measured states shows that there are always several "intermediate states" which lead via different autoionization modes to the same set of final charge states (q,Q). As an example, Table I lists all possible processes that lead, via different intermediate states, to the same set of final charge states $(q,Q)=(5+,7+)$. In Table I the collision partner which carries the K vacancy after the collision is marked with a (K), while an asterisk indicates an excited outer-shell state which is expected to decay via autoionization. Furthermore, it is assumed that the K vacancy always decays via autoionization. The subscript on the symbols for the autoionization electrons lost after the collision indicates from which collision partner (P or T) and by which shell vacancy (K or outer) they are emitted. The table shows that in three of the six possible processes that lead to the final charge-state combination $(q,Q)=(5+,7+)$ the K vacancy is transferred to the target, while in the remaining three cases it stays in the projectile. Thus every set of final charge states (q,Q) arises from a superposition of a group of "intermediate states" in which the K vacancy is transferred to the target, with another group where it remains in the projectile. Assuming that L- and K-shell charge exchange are independent processes, one can write the probability for every intermediate state as a product of the probabilities for the L-shell charge exchange P_{ou} and for the K-vacancy transfer P_{KK}. (The symbol P_{ou} is used here to indicate that electrons from the target L shell are transferred not only into the projectiles L shell, but also in outer states of the projectile. Also, target electrons can be excited in outer states during the collision.) For the example of the final charge states $(q,Q)=(5+,7+)$, Table II shows a list of the probabilities for all "intermediate states." (It is emphasized that the P_{KK} term is expected to cause the θ-dependent oscillation structure.)

TABLE II. The left column lists all possible intermediate processes that lead to the final charge-state combination $(q,Q)=(5+,7+)$ or $(7+,5+)$. In the right column the probability for each intermediate state is written as a product of the outer-shell charge-exchange probability P_{ou} and the probability of either K-vacancy transfer (P_{KK}) or the remainder of the K vacancy in the projectile ($1-P_{KK}$). The nomenclature is equivalent to the one used in Table I.

Intermediate state	Probability
	$(q,Q)=(5+,7+)$
$Ne_P^{6+}(K)+Ne_T^{**3+}$	$P_{ou}(Ne_P^{5+}+Ne_T^{**3+})\ (1-P_{KK})$
$Ne_P^{*5+}(K)+Ne_T^{*4+}$	$P_{ou}(Ne_P^{*4+}+Ne_T^{*4+})\ (1-P_{KK})$
$Ne_P^{**4+}(K)+Ne_T^{5+}$	$P_{ou}(Ne_P^{**3+}+Ne_T^{5+})\ (1-P_{KK})$
$Ne_P^{7+}+Ne_T^{**2+}(K)$	$P_{ou}(Ne_P^{7+}+Ne_T^{**1+})P_{KK}$
$Ne_P^{*6+}+Ne_T^{*3+}(K)$	$P_{ou}(Ne_P^{*6+}+Ne_T^{*2+})\ P_{KK}$
$Ne_P^{**5+}+Ne_T^{4+}(K)$	$P_{ou}(Ne_P^{**5+}+Ne_T^{3+})\ P_{KK}$
	$(q,Q)=(7+,5+)$
$Ne_P^{4+}(K)+Ne_T^{**5+}$	$P_{ou}(Ne_P^{3+}+Ne_T^{**5+})\ (1-P_{KK})$
$Ne_P^{*3+}(K)+Ne_T^{*6+}$	$P_{ou}(Ne_P^{*2+}+Ne_T^{*6+})\ (1-P_{KK})$
$Ne_P^{**2+}(K)+Ne_T^{7+}$	$P_{ou}(Ne_P^{**1+}+Ne_T^{7+})\ (1-P_{KK})$
$Ne_P^{5+}+Ne_T^{**4+}(K)$	$P_{ou}(Ne_P^{5+}+Ne_T^{**3+})\ P_{KK}$
$Ne_P^{*4+}+Ne_T^{*5+}(K)$	$P_{ou}(Ne_P^{*4+}+Ne_T^{*4+})\ P_{KK}$
$Ne_P^{**3+}+Ne_T^{6+}(K)$	$P_{ou}(Ne_P^{**3+}+Ne_T^{5+})\ P_{KK}$

The statement of Table II can be generalized to the following expression:

$$P(q,Q,\theta)=P_{KK}(\theta)\left[\sum P_{ou}(\theta)\right]_T+(1-P_{KK})\left[\sum P_{ou}(\theta)\right]_P . \quad (9)$$

A comparison of Eq. (9) with Table II shows that $[\sum P_{ou}(\theta)]_P$ describes the sum of the outer-shell charge-transfer probabilities over all possible intermediate states which are related with the remainder of the K vacancy in the projectile, while $[\sum P_{ou}(\theta)]_T$ describes the corresponding sum that is related with the K-vacancy transfer into the target. It is obvious that in the case of $[\sum P_{ou}(\theta)]_T=[\sum P_{ou}(\theta)]_P$, $P(q,Q,\theta)=[\sum P_{ou}(\theta)]_{P/T}=\sum P_{ou}(\theta)$. In this case the P_{KK} term cancels out and no oscillation structure can be observed.

One concludes that $P(q,Q,\theta)$ can show the KK interference structure if either $[\sum P_{ou}(\theta)]_T \gg [\sum P_{ou}(\theta)]_P$ or $[\sum P_{ou}(\theta)]_P \ll [\sum P_{ou}(\theta)]_T$. For every final charge-state combination, the size of each particular $P_{ou}(\theta)$ can roughly be estimated on the basis of the results of the $Ne^{7+}+Ne$ experiment. There it was shown that for projectile scattering angles θ larger than about 12 mrad the distance of closest approach is small enough that target and projectile undergo a complete equilibration of their L and outer shells. Thus each partner ends with the same mean charge state of $q=Q=4+$. Therefore, in the present measurement, it is justified to argue that for the scattering angle range between $\theta=12$ and 75 mrad, the multiple outer-shell charge exchange probability can be calculated from binomial statistics. This decreases strongly (see Ref. [23]) with increasing asymmetry of the

intermediate outer-shell charge states of projectile and target. Thus for the present experiment the relative strength of $[\sum P_{ou}(\theta)]_T$ and $[\sum P_{ou}(\theta)]_P$ can be estimated by determining the differences between the particular outer-shell charge states of projectile and target. For the example of final charge states $(q,Q)=(5+,7+)$. Table I shows that for processes *a*, *b*, and *c* the *K* vacancy remains in the target. The intermediate outer-shell charge-state differences between projectile and target for *a*, *b*, and *c* are 2, 0, and 2, respectively, which add up to the sum $S_P=4$. The corresponding outer-shell charge-state differences for the three processes *d*, *e*, and *f* (where the *K* vacancy is transferred into the target) are 6, 4, and 2, respectively, yielding a sum of $S_T=12$. According to the argument above, a decrease of S_T or S_P indicates an increased probability of *K*-vacancy transfer into the target or of remaining in the projectile, respectively. It is helpful to define the parameter γ as the ratio of the smaller to the larger of the pair S_T, S_P. For the example above we obtain $S_P/S_T=\frac{4}{12}=\frac{1}{3}$. The smaller γ is for a set of final charge states (q,Q), the more dominant is either the "P_{KK} group" or the "$(1-P_{KK})$ group" of the intermediate states and the more likely $P(q,Q,\theta)$ will show interference effects.

A comparison of the two final charge-state combinations $(q,Q)=(5+,7+)$ and $(q,Q)=(7+,5+)$ confirms that our measurements can be understood with the above analysis procedure. Both states have the same, relatively small $\gamma=\frac{1}{3}$, so that a *KK*-oscillation structure of about the same strength is expected to be seen in the data. Table II shows that the same group of intermediate states that is associated with P_{KK} in the $(q,Q)=(5+,7+)$ case belongs to $(1-P_{KK})$ in the $(7+,5+)$ case. Since the factors P_{KK} and $(1-P_{KK})$ produce an inverse oscillation structure, we expect that $P(5,7,\theta)$ and $P(7,5,\theta)$ must display this relationship. Figure 12 shows the $P(\theta)$ spectra for these two charge-state combinations. The expected behavior is observed. The very same analysis can also be done for the charge-state combinations $(q,Q)=(5+,6+)$ and $(6+,5+)$. As can be seen in Fig. 13, the $P(\theta)$ spectra of these two charge-state combinations also show an inverse oscillation structure.

Table III lists the γ values of all observed final charge-state combinations. The γ values of those combinations where the $P(q,Q,\theta)$ show oscillation structures are summarized in group *A*. Group *B* contains the γ values of those (q,Q) sets where oscillations were not observed. The average γ value of group *A* is $\gamma_a=0.27$, while in group *B* the average γ value is $\gamma_a=0.56$. Although the average γ value in group *B* is more than two times larger than the one in group *A*, three final charge-state combinations $[(q,Q)=(4+,8+)$, $(4+,7+)$, and $(3+,7+)]$ in group *B* have γ values that are small enough that one would expect some oscillation in $P(\theta)$. It is not clear why oscillations in the spectra of these combinations were not observed. It seems that a low γ value is necessary for the appearance of oscillation structures but not sufficient. Nevertheless, the γ values of the remaining 11 final charge-state combinations show a clear tendency which confirms the qualitative analysis described above.

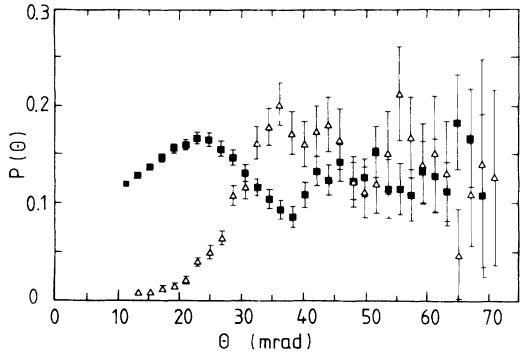

FIG. 12. $P(q,Q,\theta)$ vs projectile scattering angle for the two final charge-state combinations $(q,Q)=(5+,7+)$ (closed squares) and $(7+,5+)$ (open triangles).

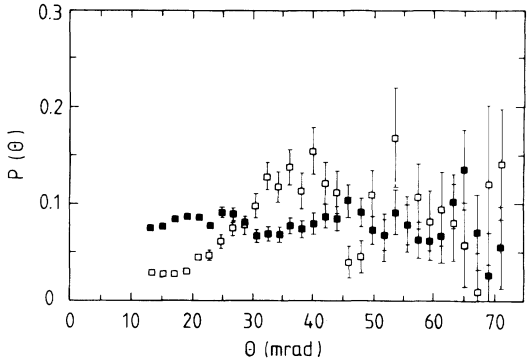

FIG. 13. Same as Fig. 12 but for the two final charge-state combinations $(q,Q)=(5+,6+)$ (solid squares) and $(6+,5+)$ (open squares).

TABLE III. List of γ values of all final charge-state combinations. Those final charge-state combinations where $P(q,Q,\theta)$ show oscillation structures are summarized in group *A*, while group *B* contains the (q,Q) combinations where oscillations in the associated probabilities cannot be observed. γ_a describes the average γ value of each group.

(q,Q)	γ
Group *A*, $\gamma a=0.27$	
5+,7+	0.33
4+,6+	0
5+,6+	0.33
6+,5+	0.33
7+,5+	0.33
Group *B*, $\gamma a=0.56$	
3+,8+	0.43
4+,8+	0.33
5+,8+	0.4
3+,7+	0.3
4+,7+	0.2
6+,6+	1.0
7+,6+	0.67
5+,5+	1.0

Finally, we would like to mention that Kürpick *et al.* [34] have calculated the *KK* charge-transfer probability for the present system by using a coupled channel method. Their calculations can reproduce fairly well the measured positions of maxima and minima in the spectra of those final charge-state combinations in which—according to the analysis above—the *K* vacancy was transferred. Thus the following final statements can be made.

The observed oscillation structures in some $P(q,Q,\theta)$ can be explained by the *KK*-vacancy-transfer mechanism together with the assumption that *K*- and *L*-shell charge transfer are independent processes. In this model, the appearance of interference structures occurs for those final charge-state combinations that arise from intermediate states whose outer-shell populations are nearly equal, for the *K*-vacancy transfer channels, and are unequal for the nontransfer channels (or vice versa). Alternatively, the selective appearance of the *KK*-interference structure may be taken as a strong indication of independent *K*-

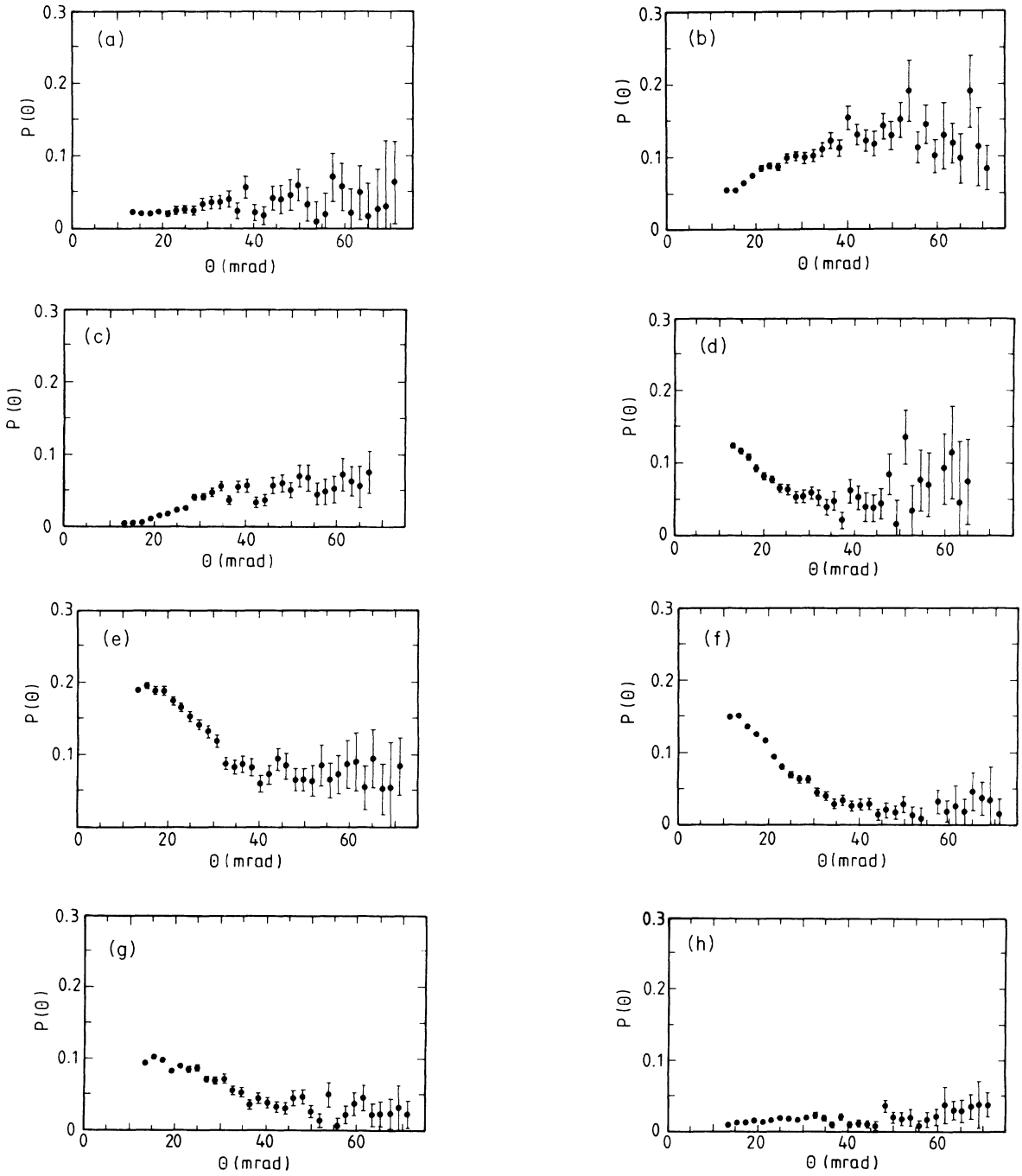

FIG. 14. $P(q,Q,\theta)$ vs θ of all measured final charge-state combinations, where oscillation structures cannot be observed. (a) $q=5+$, $Q=5+$. (b) $q=6+$, $Q=6+$. (c) $q=7+$, $Q=6+$. (d) $q=3+$, $Q=7+$. (e) $q=4+$, $Q=7+$. (f) $q=3+$, $Q=8+$. (g) $q=4+$, $Q=8+$. (h) $q=5+$, $Q=8+$.

and L-shell charge transfer.

We summarize the results of the presented investigation in the following points: (i) For projectile scattering angles larger than about $\theta=46$ mrad a 90-keV Ne^{9+} projectile and a Ne target atom undergo a complete equilibration of their atomic shells. (ii) K- and L-shell charge transfer occur independently of each other. (iii) The rotational coupling amplitude between the $2p\sigma$ and $2p\pi$ quasimolecular orbitals is negligibly small. (iv) The KK-interference effect is clearly observable for certain final charge-state pairs, indicating that the different L- and outer-shell occupations on the incoming and outgoing parts of the trajectory do not influence seriously the strength of the $1s\sigma$-$2p\sigma$ radial coupling.

ACKNOWLEDGMENTS

The experiment was performed at the electron-cyclotron-resonance ion source of the 88-in cyclotron at Lawrence Berkeley Laboratory (LBL) of the University of California at Berkeley. The authors acknowledge the assistance of the workshop in LBL Bldg. 88 and other members of the LBL 88-in cyclotron staff. Support for this work was provided by the Deutsche Forschungsgemeinschaft (R.H., R.D., H.S.-B.) and by the Director, Office of Energy Research, Office of Basic Energy Sciences, Chemical Sciences Division (M.H.P.), Division of Nuclear Physics of the Office of High Energy and Nuclear Physics (C.M.L.), U.S. Department of Energy, under Contract No. DE-AC03-76SF-00098.

APPENDIX

The $P(q,Q,\theta)$ versus θ spectra of those final charge-state combinations (q,Q) where oscillation structures cannot be observed are shown in Figs. 14(a)–14(h).

[1] B. C. Fawcett, Supplement to Z. Phys. D **21**, 1 (1991).
[2] L. Anderson, Ph.D. thesis, Manne Siegbahn Institute of Physics and Royal Institute of Technology, Stockholm, 1991.
[3] A. Niehaus, J. Phys. B **19**, 2925 (1986).
[4] A. Niehaus, Nucl. Instrum. Methods B **23**, 17 (1987).
[5] M. Barat, D. Dhuicq, R. Francois, R. McCarroll, R. D. Piacentini, and A. Salin, J. Phys. B **5**, 1343 (1972).
[6] R. K. Janev and H. Winter, Phys. Rep. **117**, 265 (1985).
[7] E. Salzborn and A. Mueller, in *Abstracts of the Eleventh International Conference on the Physics of Electronic and Atomic Collisions, Kyoto, 1979,* edited by K. Takayanagi and N. Oda (The Society for Atomic Collisions Research, Kyoto, 1979).
[8] R. Schuch, in *Invited Papers of the Fourteeth International Conference on the Physics of Electronic and Atomic Collisions, Palo Alto, 1985,* edited by D. C. Lorents, W. E. Meyerhof, and J. R. Peterson (North-Holland, Amsterdam, 1986).
[9] R. Shakeshaft and L. Spruch, Rev. Mod. Phys. **51**, 369 (1979).
[10] H. Ryufuku, K. Sasaki, and T. Watanabe, Phys. Rev. A **21**, 745 (1980).
[11] U. Fano and W. Lichten, Phys. Rev. Lett. **14**, 627 (1965).
[12] U. Wille and R. Hippler, Phys. Rep. **132**, 129 (1986).
[13] W. D. Sepp, D. Kolb, W. Sengler, H. Hartung, and B. Fricke, Phys. Rev. A **33**, 3679 (1986).
[14] V. V. Afrosimov, Yu. S. Gordeev, M. N. Panov, and N. V. Fedorenko, Zh. Tekh. Fiz. **34**, 1613 (1964) [Sov. Phys.—Tech. Phys. **9**, 1248 (1965)].
[15] Q. C. Kessel and E. Everhardt, Phys. Rev. **146**, 16 (1966).
[16] Q. C. Kessel, M. P. McCaughey, and E. Everhardt, Phys. Rev. Lett. **16**, 1189 (1966).
[17] B. Fastrup, G. Hermann, and Q. C. Kessel, Phys. Rev. Lett. **27**, 771 (1971).
[18] J. S. Briggs and J. Macek, J. Phys. B **5**, 579 (1972).
[19] R. K. Cacak, Q. C. Kessel, and M. E. Rudd, Phys. Rev. A **2**, 1327 (1970).
[20] W. E. Meyerhof, Phys. Rev. Lett. **31**, 1341 (1973).
[21] W. Aberth, D. C. Lorents, R. P. Marchi, and F. T. Smith, Phys. Rev. Lett. **14**, 776 (1965).
[22] B. Kraessig, A. Gonzales, R. Koch, T. Quinteros, A. Skutlartz, and S. Hagmann, J. Phys. (Paris) Colloq. **50**, C1-159 (1989).
[23] H. Schmidt-Böcking, M. H. Prior, R. Dörner, H. Berg, J. O. K. Pedersen, C. L. Cocke, M. Stöckli, and A. S. Schlachter, Phys. Rev. A **37**, 4640 (1989).
[24] R. Schuch, G. Nolte, H. Schmidt-Böcking, and W. Lichtenberg, Phys. Rev. Lett. **43**, 1104 (1979).
[25] R. Schuch, H. Ingwersen, E. Justiniano, H. Schmidt-Böcking, M. Schulz, and F. Ziegler, J. Phys. B **17**, 2319 (1984).
[26] F. P. Ziemba, G. J. Lockwood, G. H. Morgan, and E. Everhardt, Phys. Rev. **118**, 1552 (1960).
[27] C. Lockwood, A. Helbig, and E. Everhardt, Phys. Rev. **132**, 2078 (1963).
[28] E. Everhardt, Phys. Rev. **132**, 2083 (1963).
[29] R. Schuch, H. Ingwerson, E. Justiniano, H. Schmidt-Böcking, M. Schulz, and F. Ziegler, Nucl. Instrum. Methods A **10/11**, 75 (1985).
[30] S. Hagmann, S. Kelbch, H. Schmidt-Böcking, C. L. Cocke, P. Richard, R. Schuch, A. Skutlartz, J. Ullrich, B. Johnson, M. Meron, K. Jones, D. Trautmann, and F. Rösel, Phys. Rev. A **36**, 2603 (1987).
[31] M. Schulz, E. Justiniano, J. Konrad, R. Schuch, and A. Salin, J. Phys. B **20**, 2057 (1987).
[32] T. Kambara, Y. Awaya, Y. Kanai, R. Dörner, and H. Schmidt-Böcking, Supplement to Z. Phys. D **21**, 295 (1991).
[33] U. Wille (private communication).
[34] P. Kürpick, D. Heinemann, W.-D. Sepp, and B. Fricke, Z. Phys. D **22**, 407 (1991).

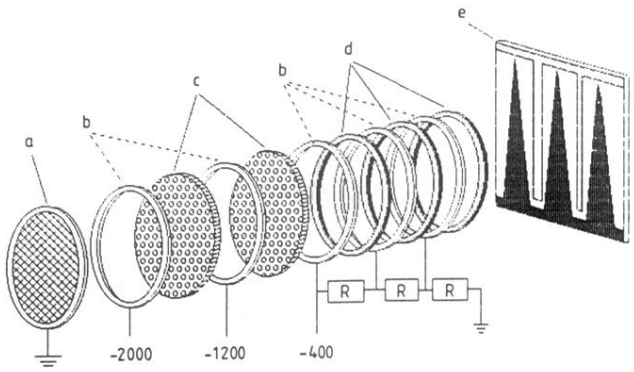

FIG. 3. Sketch of the projectile detector. *a*, grid; *b*, potential rings; *c*, microchannel plates; *d* insulating rings; *e*, wedge and strip anode.

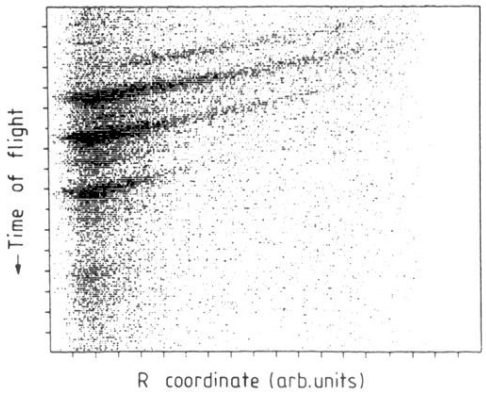

FIG. 4. Two-dimensional projection spectrum of target-recoil-ion time of flight vs projectile R coordinate on the microchannel plate detector for the final projectile charge state $Q=7+$. ($R=L\tan\Theta$, where L describes the distance between gas target and projectile detector.)

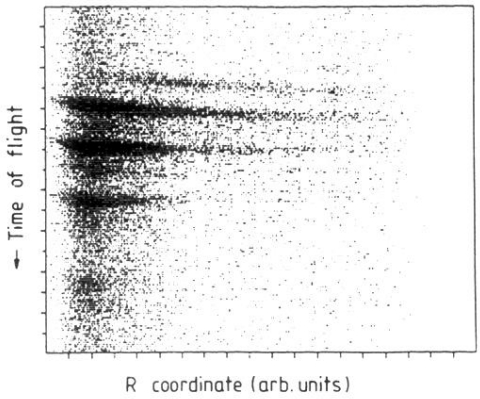

FIG. 5. Same as Fig. 4, except the TOF coordinate is shifted to smaller values of the R coordinate to correct for the R-dependent momentum transfer from the projectiles to the target ions (see text).